Vol. 47 No. SIG 9(CVIM 14) IPSJ Transactions on Computer Vision and Image Media June 2006

Regular Paper

Shape Estimation of Transparent Objects by Using Polarization Analyses

DAISUKE MIYAZAKI[†] and KATSUSHI IKEUCHI[†]

Recently, techniques developed in the field of computer graphics and virtual reality have been applied to many environments, with the result that measuring the 3D shapes of real objects has become increasingly important. However, few methods have been proposed to measure the 3D shape of transparent objects such as glass and acrylics. In this paper, we introduce three methods that estimate the surface shape of transparent objects by using polarization analysis. The first method determines the surface shape of a transparent object by using knowledge established in the research field of thermodynamics. The second method determines the surface shape of a transparent object by using knowledge established in the research field of differential geometry. The third method gives an initial value of the surface shape and then determines the true surface shape of a transparent object by iterative computation. At the end of the paper, we discuss the advantages and the disadvantages of these three methods.

1. Introduction

In the field of computer vision, few methods have been proposed for estimating the shape of transparent objects, because of the difficulty of dealing with the internal interreflection (internal reflection or interreflection), which is the phenomenon that the light not only reflects at the surface of the transparent object but also transmits into the object and causes multiple reflection and transmission inside it. This paper presents three methods for estimating the surface shape of transparent objects by analyzing the polarization of transparent objects.

1.1 Related Work

Polarization is a phenomenon in which the light oscillates in one direction. Recently, considerable research has been conducted to estimate the shape of an object by using polarization. Koshikawa and Shirai 1) proposed to use the degree of polarization, employing circulary polarized light sources to determine the surface normal of specular polyhedrons. They used a method called Mueller calculus to calculate the polarization state of the light. Wolff and Boult 2) indicated that the surface normal of the object's surface is constrained by analyzing the polarization of the object, and estimated the surface normal of a planar glass from two views. Rahmann 3) estimated the orientation of a flat object and the position of the light source by polarization analysis of a single view. Rahmann 4) also addressed the potential of recovering the shape of specular surfaces from polarization. Later, Rahmann and Canterakis 5) estimated the shape of specular objects from two or more views. Also, they proved that the quadratic shape of specular objects can be estimated from two views 6). Drbohlav and Šára 7) estimated the shape of diffuse objects by combining polarization analysis and photometric stereo. Miyazaki, et al. 8) estimated the shape and reflectance of specular objects and the illuminant direction from one view. Saito, et al. 9) employed the analysis of the degree of polarization and developed a method with which the surface of a transparent object could be determined; however, the degree of polarization provided two candidates of surface normal, and they did not solve this ambiguity. They chose the correct surface normal from a prior clue given from a human knowledge. Unfortunately, because these methods do not consider internal interreflections, they do not provide sufficient accuracy for estimating the shape of transparent objects.

A few methods that estimate the 3D shape of transparent objects have been proposed. Murase 10) estimated the shape of water surface by analyzing the undulation of the water surface. Hata, et al. 11) estimated the surface shape of transparent objects by analyzing the deformation of the light projected onto the transparent objects. Ohara, et al. 12) estimated the depth of the edge of a transparent

---

[†] Institute of Industrial Science, The University of Tokyo

object by using shape-from-focus. Ben-Ezra and Nayar[13)] estimated the parameterized surface shape of transparent objects by using structure-from-motion. Kutulakos, et al.[14),15)] estimated both the depth and the surface normal of transparent objects by multiple viewpoints and multiple light sources. These methods, however, do not estimate arbitrary shapes of transparent objects.

1.2 Overview

Saito, et al.[9)] employed analysis of the degree of polarization and developed a method with which to measure the surface of a transparent object. Then, by measuring the DOP (degree of polarization) of a transparent object, they determined surface normals. Unfortunately, however, the DOP provides two solutions corresponding to one DOP.

We will introduce two methods that removed the ambiguities from these two solutions. The first method employs the DOP of the thermal radiation, and the second method employs polarization analysis by considering the differential-geometrical property of the object surface. Saito's method and these two methods do not consider the effect of internal interreflection; hence, we introduce the third method, which estimates the surface shape of transparent objects more precisely by considering both reflection and transmission.

First method In Section 3, we explain how to analyze the thermal radiation of thermodynamics and optics to obtain the correct surface normal and thus solve the ambiguity problem.

Second method In Section 4, we explain how to solve the ambiguity problem by rotating the object and analyzing the differential-geometrical property of the surface. This method requires observing the object in a visible light domain, which is a different approach from the method in Section 3. However, the purpose of both the first method and the second method is to solve the ambiguity problem. The first method is more robust than the second method; however, the first method cannot measure ice or jelly because it requires the object to be heated.

Third method The two methods described in Section 3 and Section 4 focus on solving the ambiguity problem. However, these methods do not focus on solving the internal interreflection problem; they consider the reflection, but they do not consider the transmission. The method in Section 5 focuses on solving this internal interreflection problem by considering both reflection and transmission. The third method produces a more precise result than other two methods by only observing the visible light from one direction. However, it does not solve the ambiguity problem, and it requires an initial state of the shape.

The paper is organized as follows. In Section 2, we present the background theory of polarization and then develop an underlying algorithm to determine surface normal up to two possible zenith angles, using polarization. We explain our three methods in Section 3–5, one for each section. In Section 6, we describe the apparatus of these three methods and the experimental results obtained from using them. Section 7 discusses these three methods and Section 8 concludes the paper.

2. Polarization Analysis

2.1 Fresnel Reflection

In this section, we present a brief overview of the basic equation of reflection and refraction[16)]. In **Fig. 1**, let us consider the case in which a light hits the interface surface between two materials, the refractive indices of which are denoted as n_1 and n_2, respectively. One part of the light is reflected from the interface surface, while another part penetrates the surface and is refracted when it enters the second material. The plane including the surface normal and the incident light ray is called the POI (plane of incidence). We identify the parallel and perpendicular components to the POI as $\|$ and $\perp$, respectively. The incident, reflecting, and transmitting angles are defined as θ_1, θ_1', and θ_2, respectively, as shown in Fig. 1. Since we focus on optically smooth transparent objects, the incident angle and the reflecting angle will be the same: $\theta_1 = \theta_1'$. θ_1 and θ_2 are related

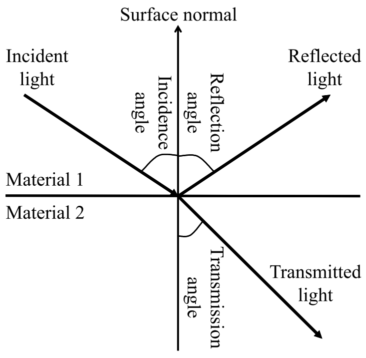

Fig. 1 Reflection, refraction, and transmission.

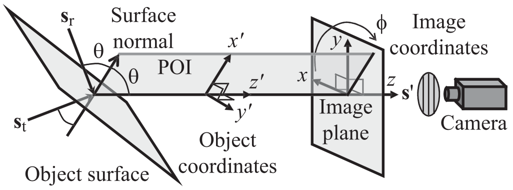

Fig. 2 Reflected and transmitted light observed by the camera.

by Snell's law,

$$n_1 \sin\theta_1 = n_2 \sin\theta_2 \,. \tag{1}$$

We define the parallel and perpendicular intensity reflectivities, $R_\parallel$ and $R_\perp$, respectively, as

$$R_\parallel = \frac{\tan^2(\theta_1-\theta_2)}{\tan^2(\theta_1+\theta_2)}$$
$$R_\perp = \frac{\sin^2(\theta_1-\theta_2)}{\sin^2(\theta_1+\theta_2)} \,. \tag{2}$$

The parallel and perpendicular intensity transmissivities, $T_\parallel$ and $T_\perp$, respectively, are defined as

$$T_\parallel = 1 - R_\parallel \,, \quad T_\perp = 1 - R_\perp \,. \tag{3}$$

From Eq. (2), an incident angle to make $R_\parallel = 0$ can be obtained. This incident angle is referred to as the Brewster angle, θ_B. The Brewster angle is obtained by substituting $\theta_1 + \theta_2 = \pi/2$ (namely, $R_\parallel = 0$) into Snell's equation as

$$\tan\theta_B = \frac{n_2}{n_1} \,. \tag{4}$$

Once the reflecting angle and the POI angle are known, we can determine the surface normal with respect to the viewer, as shown in **Fig. 2**. We will denote the POI angle and the reflecting angle as ψ and θ, respectively, and determine these two angles by using the degree of polarization of reflected light, as shown in the subsequent sections.

2.1.1 POI Angle

As shown in Eq. (2), the intensity of the reflected light varies depending on the direction of oscillation in the plane of oscillation; therefore, a difference can be observed when the polarization filter is rotated in front of a CCD camera. The variance is described as a sinusoidal function of rotation angles. We will denote the maximum and minimum brightness in the observed intensities as $I_{\max}$ and $I_{\min}$. Given that the sum of the maximum and minimum brightness is the total brightness of the reflected light I_{spec},

$$I_{\max} = \frac{R_\perp}{R_\parallel + R_\perp} I_{\text{spec}}$$
$$I_{\min} = \frac{R_\parallel}{R_\parallel + R_\perp} I_{\text{spec}} \,, \tag{5}$$

since $R_\perp(\theta_1) \geq R_\parallel(\theta_1)$ holds for any θ_1.

By this equation, the direction parallel to the plane of incidence provides the minimum brightness $I_{\min}$. Namely, by measuring the angle where the minimum brightness is observed, we can determine the POI angle ψ ($0 \leq \psi < 2\pi$). POI angle is determined as the angle between $+x$-axis and POI, from $+x$-axis to $+y$-axis, as shown in Fig. 2. There are two possible POI angles, ψ_{LO} and ψ_{HI}, which are definable as $\psi_{\text{HI}} = \psi_{\text{LO}} + \pi$, where $0 \leq \psi_{\text{LO}} < \pi$ and $\pi \leq \psi_{\text{HI}} < 2\pi$. Surface normal can be represented in polar coordinates with zenith angle θ and azimuth angle ϕ. Azimuth angle ϕ equals to ψ_{LO} or ψ_{HI} if there is no internal interreflection.

Since we assume that the object is a closed, smooth object, we can determine the surface normal at the occluding boundary; the surface normal heads for the outside of the shape of the projection of the object at the occluding boundary. By using the ϕ at the occluding boundary as an initial condition, we propagate the constraint of ϕ throughout the surface and, finally, determine the value of ϕ, whether it is $\phi = \psi_{\text{LO}}$ or $\phi = \psi_{\text{HI}}$, over the entire surface, assuming that all local parts of the surface are not concave toward the camera direction.

The first method described in Section 3 and the second method described in Section 4 use this procedure to determine the azimuth angle ϕ. These two methods only consider the reflection and do not consider the transmission. Therefore, the third method described in Section 5 refines the azimuth angle by considering the transmission.

2.1.2 Incident Angle

The definition of the degree of polarization is

$$\rho = \frac{I_{\max} - I_{\min}}{I_{\max} + I_{\min}} \,. \tag{6}$$

The degree of polarization is 0 when the light is unpolarized, whereas it is 1 when the light is linearly polarized. The linearly polarized light is observed when the incident angle and the reflecting angle are at the Brewster angle.

By substituting Eqs. (5) and (2) into Eq. (6) with Snell's law, we can represent the degree of polarization ρ as

$$\rho = \frac{2\sin^2\theta\sqrt{n^2 - \sin^2\theta - n^2\sin^2\theta + \sin^4\theta}}{n^2 - \sin^2\theta - n^2\sin^2\theta + 2\sin^4\theta} \,, \tag{7}$$

if we consider only the reflection and do

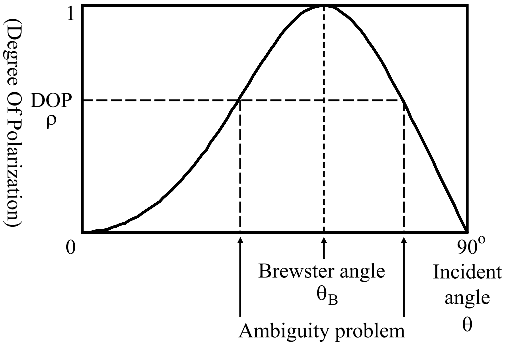

Fig. 3 Relation between the degree of polarization and the incident angle ($n = 1.5$).

not consider the transmission. The degree of polarization is a function of the refractive index n $(= n_2/n_1)$ and the incident angle θ $(= \theta_1)$ $(0 \leq \theta \leq \pi/2)$. Threfore, by obtaining the degree of polarization from the data, we can determine the incident angle θ, given the refractive index n.

Figure 3 shows the relationship between the degree of polarization and the incident angle. Here, the horizontal and vertical axes denote the incident angle and the degree of polarization, respectively. We can obtain the incident angle from the observed degree of polarization even if we do not know the intensity of the light source. The function has an extremum at the Brewster angle. From this function, an observed degree of polarization provides two possible incident angles, except at the Brewster angle. It is necessary to have a method to resolve this ambiguity. In this paper, we propose to solve this problem by two methods, one by considering the polarization of far infrared light (Section 3), and the other by comparing two polarization data sets through rotating the object (Section 4). The unique zenith angle θ is determined by these two methods if there is only the reflection and there is no transmission. The true zenith angle is obtained by the third method described in Section 5, which considers both reflection and transmission.

2.2 Polarization Raytracing

In this section, we present the technique that calculates the polarization state of the light. This technique not only considers the reflection but also considers the transmission. It is used in the third method described in Section 5.

2.2.1 Mueller Calculus

A conventional raytracing method renders a 2D image from 3D geometrical shape data of transparent objects or other kind of objects. In this paper, we call the raytracing method that considers the polarization effect the polarization raytracing method. The algorithm of the polarization raytracing method can be divided into two parts. For the first part, the calculation of the propagation of the ray, we employ the same algorithm used in the conventional raytracing method. For the second part, the calculation of the polarization state of the light, the direct implementation of Section 2.1 is possible. However, there are more effective methods to calculate the polarization: Mueller calculus[17], Jones calculus[17], and the method that uses the coherence matrix[16]. In this paper, we employ Mueller calculus, because of its simplicity of description, along with its ease of understanding and implementation. These three methods have almost identical functions; thus, all discussions presented in this paper are also applicable to other calculi. We will present a brief overview of Mueller calculus in the following pages; however, we will leave the details to the literature[17].

In Mueller calculus, the polarization state of the light is represented as Stokes vector $\mathbf{s} = (s_0, s_1, s_2, s_3)^T$. The Stokes vector is a 4D vector. Its first component s_0 represents the intensity of the light; its second component s_1 represents the horizontal power of the linear polarization; its third component s_2 represents the $+45°$-oblique power of the linear polarization; and its fourth component s_3 represents the power of the right circular polarization. The Mueller matrix $\mathbf{M}$, which is a 4×4 matrix, represents how the object changes the polarization state of the light. The operation of Mueller calculus is a linear operation.

2.2.2 Mueller Matrix

First, we introduce a method for calculating the polarization state of the reflected light and the transmitted light when the POI angle is 0°; after that, we introduce a method for the case when the POI angle is not 0°.

Mueller Matrices of reflection $\mathbf{R}$ and transmission $\mathbf{T}$ when the POI angle is 0° are represented as follows:

$$\mathbf{R} = \begin{pmatrix} (R_\parallel + R_\perp)/2 & (R_\parallel - R_\perp)/2 & 0 & 0 \\ (R_\parallel - R_\perp)/2 & (R_\parallel + R_\perp)/2 & 0 & 0 \\ 0 & 0 & \sqrt{R_\parallel R_\perp} & 0 \\ 0 & 0 & 0 & \sqrt{R_\parallel R_\perp} \end{pmatrix}$$

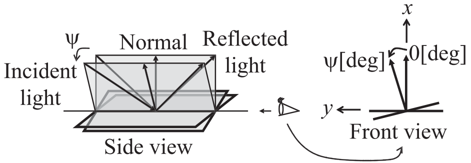

(a)POI is ψ rotated

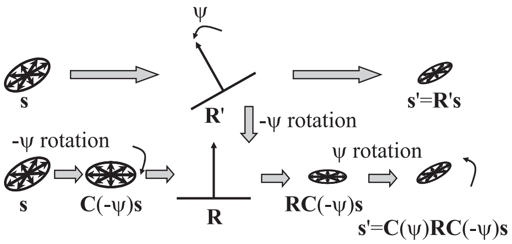

(b)Example for Mueller calculus

Fig. 4 Calculation example of rotation Mueller matrix for reflection.

$$\mathbf{T} = \begin{pmatrix} (T_{\parallel}+T_{\perp})/2 & (T_{\parallel}-T_{\perp})/2 & 0 & 0 \\ (T_{\parallel}-T_{\perp})/2 & (T_{\parallel}+T_{\perp})/2 & 0 & 0 \\ 0 & 0 & \sqrt{T_{\parallel}T_{\perp}} & 0 \\ 0 & 0 & 0 & \sqrt{T_{\parallel}T_{\perp}} \end{pmatrix}. \tag{8}$$

Therefore, if we have a light ray with the Stokes vector **s** impinged on an object, then the Stokes vector of reflected light will be **Rs**, when the POI angle is 0°. The same thing can also be said of the transmitted light.

Figure 2 illustrates the case when the POI angle is ψ. **Figure 4** explains how to calculate the reflected light for this case. The reflection matrix **R** is always multiplied to the Stokes vector whose POI angle is transformed to 0°. So, we first rotate the incident Stokes vector **s** with the angle $-\psi$. After that, **R** is multiplied to the transformed Stokes vector. Finally, the Stokes vector is rotated again with the angle ψ in order to restore the original coordinates. The resulting Stokes vector $\mathbf{s}'$ is as follows:

$$\mathbf{s}' = \mathbf{C}(\psi)\mathbf{R}\mathbf{C}(-\psi)\mathbf{s}\,, \tag{9}$$

where rotation matrix **C** is given as:

$$\mathbf{C}(\psi) = \begin{pmatrix} 1 & 0 & 0 & 0 \\ 0 & \cos 2\psi & -\sin 2\psi & 0 \\ 0 & \sin 2\psi & \cos 2\psi & 0 \\ 0 & 0 & 0 & 1 \end{pmatrix}. \tag{10}$$

As for the case in Fig. 2, observed light is a composition of reflected light and transmitted light. Therefore, the Stokes vector $\mathbf{s}'$ of the observed light is calculated as follows:

$$\mathbf{s}' = \mathbf{C}(\psi)\mathbf{R}\mathbf{C}(-\psi)\mathbf{s}_r + \mathbf{C}(\psi)\mathbf{T}\mathbf{C}(-\psi)\mathbf{s}_t, \tag{11}$$

where Stokes vectors of the incident light are represented as $\mathbf{s}_r$ and $\mathbf{s}_t$, and where $\mathbf{s}_r$ and $\mathbf{s}_t$ represent the lights that are set in the origin of the reflection and transmission, respectively.

2.2.3 Phase Shift

If an incident angle is larger than the critical angle, then the light does not transmit and totally reflects. This phenomenon is called total reflection and occurs when the light is inside the object. Critical angle is defined in following equation:

$$\sin\theta_C = \frac{n_2}{n_1}\,. \tag{12}$$

Here, n_1 and n_2 are the refractive indices of two materials, where $n_1 > n_2$; for example, n_1 and n_2 might be the refractive indices of the object and the air, respectively. Phase of the reflected light shifts when the total reflection occurs. Therefore, for the total reflection, the following matrix **D** is used instead of the reflection Mueller matrix **R**:

$$\mathbf{D}(\delta) = \begin{pmatrix} 1 & 0 & 0 & 0 \\ 0 & 1 & 0 & 0 \\ 0 & 0 & \cos\delta & \sin\delta \\ 0 & 0 & -\sin\delta & \cos\delta \end{pmatrix}, \tag{13}$$

where δ is the amount of the phase shift, calculated by using the following formula:

$$\tan\frac{\delta}{2} = \frac{\cos\theta\sqrt{\sin^2\theta - n^2}}{\sin^2\theta}\,, \tag{14}$$

where θ is the incident angle and $n = n_2/n_1$, where n_1 and n_2 are the refractive indices of the object and the air, respectively.

When the incident angle is less than the Brewster angle, the phase of the reflected light will be inverted; thus, the matrix $\mathbf{D}(180°)$ should be multiplied from the left to the reflection Mueller matrix.

2.2.4 Degree of Polarization

Because linear polarizer is used in this research, the fourth parameter s_3 of the Stokes vector cannot be determined. The relationship between the Stokes vector $(s_0, s_1, s_2)^T$ and $I_{\max}$, $I_{\min}$, ψ is:

$$\begin{pmatrix} s_0 \\ s_1 \\ s_2 \end{pmatrix} = \begin{pmatrix} 1 & 0 & 0 \\ 0 & \cos 2\psi & -\sin 2\psi \\ 0 & \sin 2\psi & \cos 2\psi \end{pmatrix} \begin{pmatrix} I_{\min} + I_{\max} \\ I_{\min} - I_{\max} \\ 0 \end{pmatrix}, \tag{15}$$

where $I_{\max}$ and $I_{\min}$ are defined in Section 2.1, and ψ is a POI angle also defined in Section 2.1. The degree of polarization represents how much the light is polarized and is defined as follows:

$$\hat{\rho} = \frac{\sqrt{s_1^2 + s_2^2 + s_3^2}}{s_0} . \tag{16}$$

However, the linear polarizer can only calculate the following DOLP (degree of linear polarization):

$$\rho = \frac{I_{\max} - I_{\min}}{I_{\max} + I_{\min}} = \frac{\sqrt{s_1^2 + s_2^2}}{s_0} . \tag{17}$$

For the remainder of this paper, we refer to the ratio calculated by Eq. (17) as the DOP.

The DOP of Eqs. (17) and (6) are the same. By considering only the reflection, we will obtain Eq. (7). The true DOP is represented by the Stokes vector as in Eq. (17) by considering both reflection and transmission. The first method (Section 3) and the second method (Section 4) analyze Eq. (7), while the third method (Section 5) analyzes Eq. (17). The value of the DOP from observation is same for both Eqs. (7) and (17); however, the inherent mathematical structure is quite different.

2.2.5 Illumination Distribution

In this paper, we assume that all light sources are unpolarized. In Section 5, we assume that the intensity of the illumination is known.

3. Shape Estimation of Transparent Objects by using Polarization Analysis and Thermal Radiation

3.1 Thermal Radiation

Any object that has a positive temperature will radiate energy. Let us explain the polarization phenomenon of thermal radiation by considering the light emitted from inside the object 18)~23). Thermal radiation generated from inside the object is transmitted through the interface surface and radiated into the air.

For the explanation in this section, suppose material 1 to be the object and material 2 to be the air in Fig. 1. In this case, $\theta_2 > \theta_1$. The refractive index of the object relative to the air will be $n = n_1/n_2$. θ_2 is the emitting angle. The emitting angle is the angle between the surface normal and the camera direction, and is the same as the zenith angle.

We can define the parallel and perpendicular intensity transmissivity, $T_\parallel$ and $T_\perp$, as

$$T_\parallel = \frac{\sin 2\theta_1 \sin 2\theta_2}{\sin^2(\theta_1 + \theta_2)\cos^2(\theta_1 - \theta_2)}$$
$$T_\perp = \frac{\sin 2\theta_1 \sin 2\theta_2}{\sin^2(\theta_1 + \theta_2)} , \tag{18}$$

derived from Eqs. (1)–(3). Therefore, $I_{\max}$ and $I_{\min}$ will be written by using the total energy of the emitted light, W, as

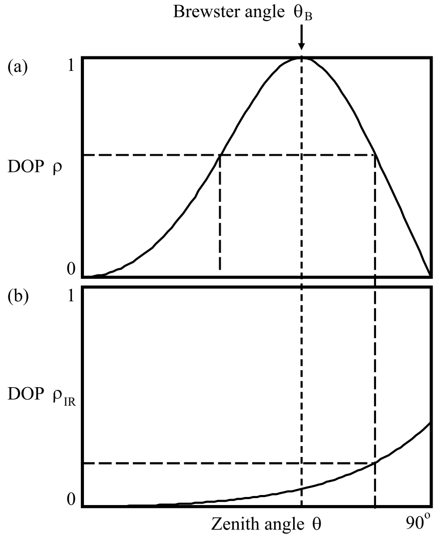

Fig. 5 DOP of (a) thermal radiation (infrared light) ($n = 1.5$), and (b) reflected light (visible light) ($n = 1.5$).

$$I_{\max} = \frac{T_\parallel}{T_\parallel + T_\perp} W$$
$$I_{\min} = \frac{T_\perp}{T_\parallel + T_\perp} W , \tag{19}$$

since $T_\parallel(\theta_2) \geq T_\perp(\theta_2)$ holds for any θ_2.

The degree of polarization of thermal radiation ρ_{IR} will be as follows:

$$\rho_{\mathrm{IR}} = \frac{I_{\max} - I_{\min}}{I_{\max} + I_{\min}} = \frac{T_\parallel - T_\perp}{T_\parallel + T_\perp} . \tag{20}$$

3.2 Degree of Polarization of Thermal Radiation

Figure 5 (a) shows the relation between the DOP, ρ_{IR}, and the emitting angle, θ. As shown in this figure, there is a 1-to-1 correspondence between the DOP and the emitting angle. Therefore, once we measure the DOP in an infrared light, we can uniquely determine the emitting angle. For the sake of comparison, Fig. 5 (b) represents the visible light condition. In this function, as mentioned, one DOP value corresponds to two emitting angles.

Unfortunately, however, the DOP in emitted infrared light is much smaller than that in reflected visible light. Thus, we propose to use both visible and infrared light. By using visible light, we can achieve a highly accurate measurement with ambiguity. By using the infrared light, we discriminate between the two sides.

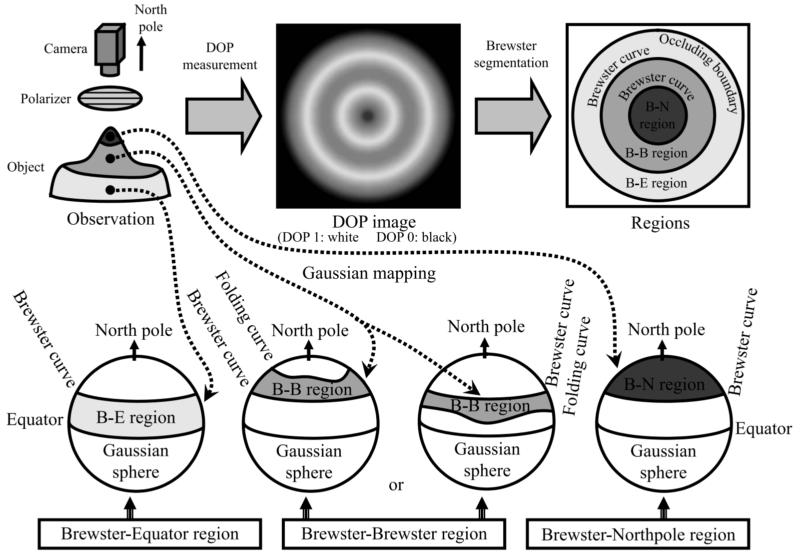

Fig. 6 Gaussian mapping and regions.

4. Shape Estimation of Transparent Objects by using Polarization Analysis and Differential Geometry

In this section, we introduce the method of solving the ambiguity by rotating the object. If the reader of this paper is not familiar to the fundamental theory of Gaussian geometry, please read the literature 24),25).

4.1 Brewster Segmentation

We have explained how to obtain the DOP of the light reflected on the object's surface in Section 2. Now, we segment the data of the DOP into regions bounded by the Brewster angle θ_B. Points of the Brewster angle have no ambiguity and the DOP ρ is equal to 1.

Since we assume that the object is a closed, smooth object, the curve connected by points of the Brewster angle will form a closed curve. This curve is sometimes thick, sometimes thin, and sometimes a combination of both. We denote a point where the zenith angle is equal to the Brewster angle as the "Brewster point" and the closed curve consisting of Brewster points as the "Brewster curve." We define the segmentation by Brewster curves as "Brewster segmentation."

The incident angle of all points in the region segmented through Brewster segmentation is either greater than the Brewster angle or smaller than the Brewster angle. Therefore, we can uniquely determine all the incident angles in the region if we can disambiguate only one point in the region.

Now, let us consider the surface regions segmented with regard to the Brewster angle with a Gaussian sphere representation. The regions generated by Brewster segmentation can be grouped into three classes (**Fig. 6**):

(1) B-E region — a region enclosed within a Brewster curve and an occluding boundary (mapped to the Equator on the Gaussian sphere),

(2) B-N region — a region enclosed only with a Brewster curve and containing a surface normal toward the viewer direction (mapped to the North Pole on the Gaussian sphere),

(3) B-B region — a region enclosed only with one or more Brewster curves, neither containing an occluding boundary or the surface normal facing the viewer.

The result of the Brewster segmentation of the object depicted in **Fig. 7** is shown in **Fig. 8**. Figure 8 (a) is a gray image of the DOP, where $\rho = 0$ is represented as black and $\rho = 1$ is represented as white. Figure 8 (b) is the result of the Brewster segmentation of Fig. 8 (a). There are two Brewster curves and one occluding boundary and one each of a B-E region, a B-B region, and a B-N region.

4.1.1 B-E Region

The B-E region is the region that includes the occluding boundary whose zenith angle θ equals 90°. On the Gaussian sphere, the B-E region is enclosed within a small circle mapped from the Brewster curve and an equator

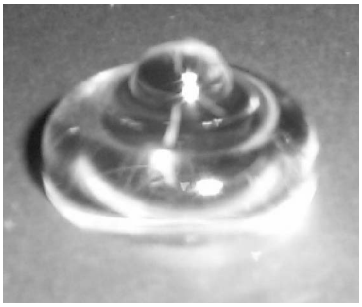

Fig. 7 A photograph of the bell-shaped object.

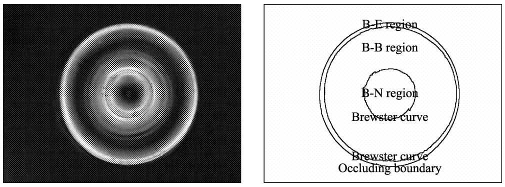

(a) (b)

Fig. 8 (a) A gray image of obtained degree of polarization of the bell-shaped object and (b) the result of Brewster segmentation.

mapped from the occluding boundary. The zenith angle of all the points of the B-E region is located between the Brewster angle and the occluding angle, 90°. The graph described in Fig. 3 indicates that the correspondence between θ and ρ is one to one at this region, $\theta_B \leq \theta \leq 90°$; thus, we can uniquely determine the incident angle from an observed DOP, ρ.

We assume that the self-occlusion never occurs even if we tilted the object at an infinitesimal angle. To satisfy the above assumptions, we consequently assume that there are no points where the zenith angle θ is equal to 90° except for the occluding boundary. By calculating the background subtraction image, the occluding boundary can be calculated; thus, the B-E region is easily determined.

4.1.2 B-N Region

The B-N region is the region that includes one or more points (this is preferable to point(s)) mapped onto the North Pole on the Gaussian sphere. As shown in Fig. 3, the region is mapped to a spherical cap on the Gaussian sphere, enclosed by a small circle mapped from the Brewster curve. The North Pole is located at the center of this spherical cap. The zenith angle of all the points in this region is in the range of $0° \leq \theta \leq \theta_B$. From the graph in Fig. 3, we can conclude that, in this range, the correspondence between θ and ρ is one to one, and we can also determine the zenith angle from the observed DOP.

If the DOP ρ equals zero, the zenith angle θ will be 0° or 90°. However, since we assume that the points where the zenith angle θ is equal to 90° only appear at the occluding boundary, the B-N region is determined only by searching the point where the degree of polarization equals zero.

4.1.3 B-B Region

The B-B region is defined as the region that includes neither the occluding boundary nor the North Pole points and is bounded by one or more Brewster curves. The region that is neither the B-E region nor the B-N region is the B-B region. In the following sections, we will propose a method for disambiguating B-B regions.

4.2 Folding Curve

There are two possibilities for the existence of the B-B region on the Gaussian sphere. The B-B region is either on the northern side of the Brewster curve or on the southern side of the Brewster curve. The B-B region mapped onto the Gaussian sphere is bounded by one Brewster curve and one or more extra curves (Fig. 6). By considering the points in the B-B region on the Gaussian sphere, we find that there is one extreme point — northernmost or southernmost — in each azimuth angle. We denote the set of these points to be a folding curve. Now, we will prove that the folding curve is a geometrical invariant; the Gaussian curvature at the folding curve will be zero.

Theorem *Any folding curve on an object's surface is a parabolic curve on that object's surface. That is to say, at any surface point on a folding curve, the Gaussian curvature at the surface point vanishes.*

Proof. A surface normal can be represented in gradient space, a space constructed by gradients p and q:

$$p = \frac{\partial H}{\partial x}\,, \quad q = \frac{\partial H}{\partial y}\,, \tag{21}$$

where $H = H(x, y)$ denotes the height of the object surface. A folding curve is an extremum not only in a Gaussian sphere, but also in gradient space, $p = p(x, y)$ and $q = q(x, y)$. Therefore, one or both of the following equations holds:

$$\frac{\partial p}{\partial x} = \frac{\partial p}{\partial y} = 0 \tag{22}$$

$$\frac{\partial q}{\partial x} = \frac{\partial q}{\partial y} = 0\,. \tag{23}$$

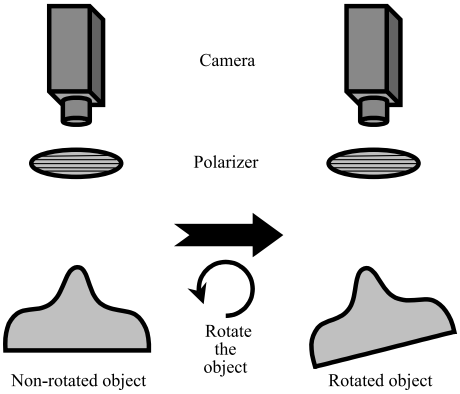

Fig. 9 Object rotation.

Hessian $\mathcal{H}$ and Gaussian curvature K are related by the following equation:

$$\operatorname{sgn} K = \operatorname{sgn} \det \mathcal{H} \,, \tag{24}$$

where Hessian is defined as:

$$\mathcal{H} = \begin{pmatrix} \dfrac{\partial^2 H}{\partial x^2} & \dfrac{\partial^2 H}{\partial x \partial y} \\ \dfrac{\partial^2 H}{\partial y \partial x} & \dfrac{\partial^2 H}{\partial y^2} \end{pmatrix} . \tag{25}$$

Since Eqs. (22) or (23) holds, from Eqs. (21)–(25), $K = 0$ is finally obtained. □

A parabolic curve is a curve where Gaussian curvature is zero and Gaussian curvature of the object's surface does not change through rotation of the object. Therefore, we can conclude that the folding curve is intrinsic to an object and invariant from the viewer direction.

4.3 Corresponding Points

We will solve the ambiguity in the B-B region by comparing the data of the DOP of a non-rotated object and that of a rotated object at a small angle (**Fig. 9**). We compare the DOP at two points where the invariant property on the surface matches, and disambiguate the ambiguity problem.

The Gaussian mapping of the B-B region of the object's surface onto the Gaussian sphere is depicted in Fig. 6. The B-B region includes neither the occluding boundary nor the north pole point, and is bounded only by the Brewster curve; thus, the folding curve always appears.

We define the corresponding point as the point where the folding curve and the great circle intersect (**Fig. 10**). This great circle must be a cross-section between the Gaussian sphere and the plane that is parallel to the rotation direction of the object and includes the north pole of the Gaussian sphere. The surface point that is mapped onto this great circle still maps onto the great circle after the object's rotation, thus enabling unique matching.

To summarize:

(1) If the B-B region is mapped onto the north of the Brewster curve, choose the northernmost point for the corresponding point that intersects the great circle; namely, choose the point where the DOP is minimum.

(2) If the B-B region is mapped onto the south of the Brewster curve, choose the nearest point to the equator for the corresponding point that intersects the great circle; namely, choose the point where the DOP is minimum.

4.4 Difference of Degree of Polarization

Finally, we describe the method used to resolve the ambiguity problem of the surface normal by comparing the DOP at the corresponding point of the nontilted object with that of the tilted object.

We regard the refractive index n as constant; thus, the DOP ρ is only a function of the zenith angle θ. The relationship between the rotation angle, $\Delta\theta$, the DOP of the nontilted object, $\rho(\theta)$, the DOP of the tilted object, $\rho(\theta + \Delta\theta)$, and the derivative of the DOP, $\rho'(\theta)$, will be:

$$\rho(\theta + \Delta\theta) - \rho(\theta) = \rho'(\theta)\Delta\theta \,, \tag{26}$$

if $\Delta\theta$ is sufficiently small.

In fact, the absolute value of the rotation angle is not needed; however, we assume that the rotation direction is known. Since the azimuth angle ϕ has also already been determined, the sign of $\Delta\theta$ can be determined. As a result, by calculating the sign of the difference of two DOP values at the corresponding point and by giving the sign of $\Delta\theta$, we can determine, by using Eq. (26), whether the zenith angle θ in the B-B region is in the range of $0 \le \theta \le \theta_B$ or of $\theta_B \le \theta \le \pi/2$ (**Fig. 11**).

5. Shape Estimation of Transparent Objects by using Polarization Raytracing

In this section, we introduce the proposed method for estimating the frontal surface shape of a transparent object using the DOP and the POI angle as inputs under the assumption that the refractive index and the backward-facing surface shape are given. Details of numerical algorithms and mathematics are shown in the literature[26),27)].

5.1 Inverse Polarization Raytracing

We denote the input polarization data as I_E. Polarization data are represented as an image

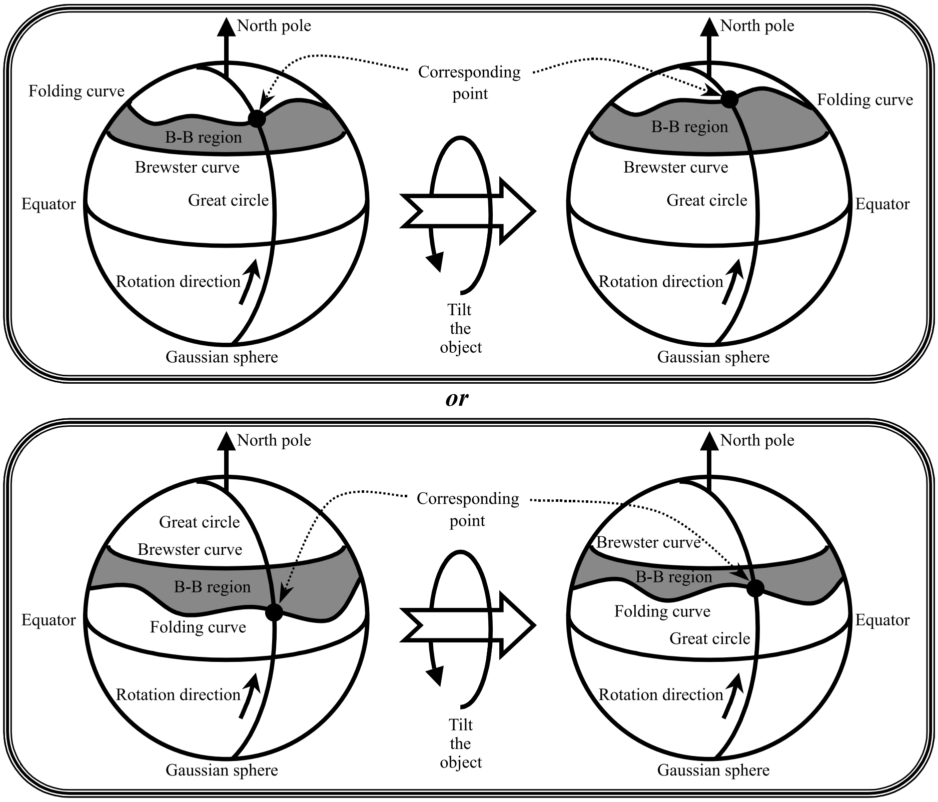

Fig. 10 Corresponding point.

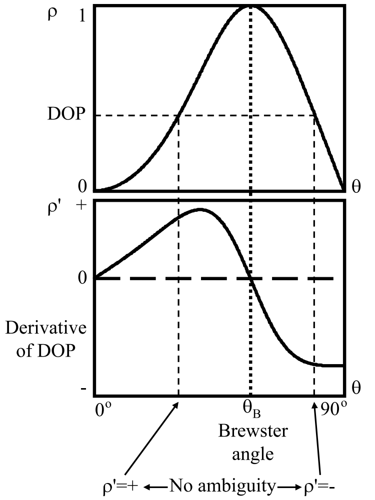

Fig. 11 Graph of derivative of DOP ($n = 1.5$).

(2-dimensionally distributed data) where the DOP and POI angle are set for each pixel. The polarizaiton raytracing explained in Section 2.2 can render the polarization data from the shape of a transparent object. We denote such rendered polarization images as I_R. The shape of transparent objects is represented as the height H, set for each pixel. Heights partially differentiated by x and y are called gradient, and are represented as p and q, respectively:

$$p = H_x = \frac{\partial H}{\partial x}, \quad q = H_y = \frac{\partial H}{\partial y}. \qquad (27)$$

Surface normal $\mathbf{n} = (-p, -q, 1)^T$ is represented by these gradients. The rendered polarization image I_R depends upon height and surface normal, so it can be represented as $I_R(H, p, q)$. A straightforward definition of the cost function that we want to minimize can be as follows:

$$\iint E_1(x, y)\, dx\, dy\,, \qquad (28)$$

where,

$$E_1 = (I_E - I_R(H, p, q))^2\,. \qquad (29)$$

We will sometimes omit the variables (x, y) in subsequent discussions for the simplicity of descriptions. I_R depends upon p, q, and H, while p, q, and H depend upon each other with Eq. (27). Therefore, the cost function must be modified as follows:

$$\iint (\lambda E_1 + E_2)\, dx\, dy\,, \tag{30}$$

where,

$$E_2 = (H_x - p)^2 + (H_y - q)^2\,. \tag{31}$$

λ is the Lagrange undetermined multiplier.

Euler equations that minimize Eq. (30) will be,

$$p = H_x - \frac{\lambda}{2}\frac{\partial E_1}{\partial p} \tag{32}$$

$$q = H_y - \frac{\lambda}{2}\frac{\partial E_1}{\partial q} \tag{33}$$

$$H = \bar{H} - \frac{1}{4}(p_x + q_y) - \frac{\lambda}{8}\frac{\partial E_1}{\partial H}\,, \tag{34}$$

where $\bar{H}$ is a 4-neighbor average of H.

Each of the above Eqs. (32), (33), (34) can be decomposed into two steps:

$$p \leftarrow H_x \tag{35}$$

$$p \leftarrow p - \lambda_1 \frac{\partial E_1}{\partial p} \tag{36}$$

$$q \leftarrow H_y \tag{37}$$

$$q \leftarrow q - \lambda_2 \frac{\partial E_1}{\partial q} \tag{38}$$

$$H \leftarrow \bar{H} - \frac{1}{4}(p_x + q_y) \tag{39}$$

$$H \leftarrow H - \lambda_3 \frac{\partial E_1}{\partial H}\,. \tag{40}$$

Here, λ_1, λ_2, and λ_3 are scalar values that are determined for each pixel and for each iteration step.

First, we set initial values of the shape H for each point of frontal surface. Next, p and q are calculated by Eqs. (35), (37). Then, we solve Eqs. (36), (38). λ_1 and λ_2 should be optimal values; thus, we use Brent's method to determine λ_1 and λ_2, which minimize the error function E_1. After computing p and q at every pixel, we solve Eq. (39) by the relaxation method [28),29)] to determine the height H. We solved the relaxation problem by using the alternating-direction implicit method.

We do not choose to solve Eq. (40) by Brent's method because the error function E_1 depends upon the change of surface normal rather than on the change of height. Another reason is that the error function E_1 smoothly changes when the surface normal changes, but it does not smoothly change when the height changes.

To conclude, the frontal surface shape of a transparent object is estimated by an iterative computation, where each step of iteration solves Eqs. (35)–(39), and the iteration stops when Eq. (28) is minimized.

6. Experiments

6.1 Experimental Setup of Visible Light

Figure 12 represents our experimental setup, which we named "Cocoon," for obtaining the polarization data in a visible light domain. The target object is set inside the center of the plastic sphere whose diameter is 35 cm. This plastic sphere is illuminated by 36 incandescent lamps. These 36 light sources are almost uniformly distributed spatially around the plastic sphere by a geodesic dome. The plastic sphere diffuses the light that comes from the light sources, and it behaves like a spherical light source, which illuminates from every direction the target object that is located at the center of the sphere. This spherical diffuser provides an unpolarized light. The target object is observed by a monochrome camera from the top of the plastic sphere, which has a hole on the top. A linear polarizer is set in front of the camera.

6.2 Experimental Setup of Infrared Light

Figure 13 shows the apparatus for infrared light. Given that infrared light is thermal radiation from a body and is not a reflection component, we do not use any light source. We increase the temperature of the object to 30–40 degrees Celsius by using a hair dryer to blow heated air over it. We also employ an infrared polarizer and an IR-CCD camera.

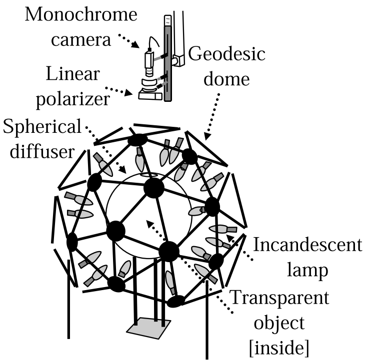

Fig. 12 Experimental setup for visible light.

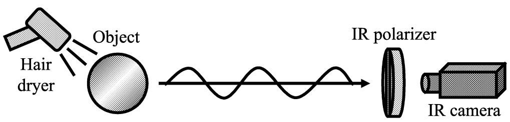

Fig. 13 Experimental setup for infrared light.

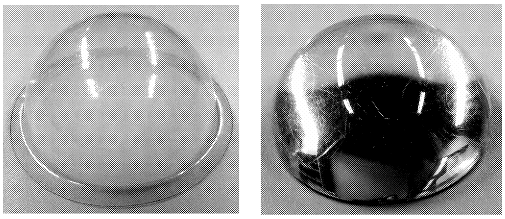

(a) (b)

Fig. 14 Photographs of acrylic hemispherical objects.

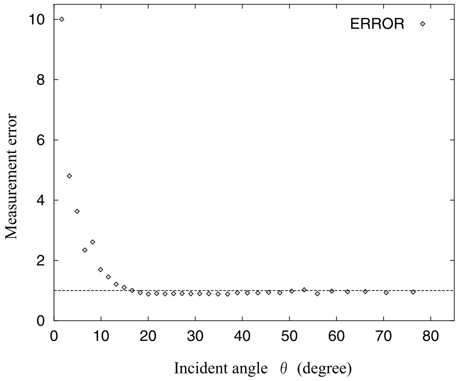

Fig. 15 Error characteristics of the spherical object.

6.3 Experimental Results of the Thermal Radiation Method

This section shows the experimental results of the first method, which uses thermal radiation.

In order to determine the accuracy of the system, we use an acrylic hemisphere having a refractive index of 1.5 and a diameter of 50 mm shown in **Fig. 14** (a). **Figure 15** shows the error characteristics from the observed measurement. The horizontal axis is the zenith angle and the vertical axis denotes the measurement errors. In the figure, the dotted straight line denotes the case without any measurement errors.

From this experiment, except around the area of small angles, the measurement error is small, and we can achieve high accuracy in measurement. One of the reasons for the relatively noisy data around the smaller angles is that the spherical diffuser has a hole in its top portion, and the object does not receive light from that area. Another reason is that the derivative of the DOP is close to zero where the incident angle is near 0°, and is less stable for determining the incident angle (zenith angle) from the DOP. The RMS error of the zenith angle was 5.9°.

Next, we determined the shape of the object shown in **Fig. 16** (a). The shellfish-shaped object is made of acrylic and its refractive index is 1.5. The refractive index was obtained from the literature[30)]. Figure 16 (b) shows the obtained shape of the object.

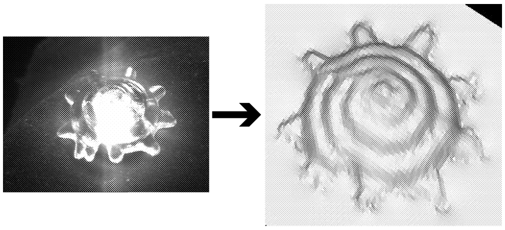

(a) Acrylic shellfish object (b) Obtained shape

Fig. 16 The resulting shape of the shellfish-shaped object.

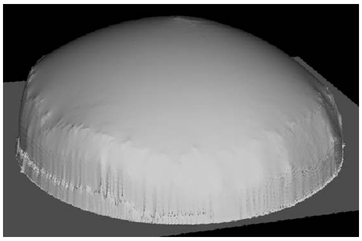

Fig. 17 A rendered image of the obtained shape of the hemispherical object.

6.4 Experimental Results of the Differential Geometry Method

This section shows the experimental results of the second method, which uses differential geometry.

First, we used an acrylic transparent hemisphere whose diameter was 30 mm, shown in Fig. 14 (b). Its refractive index was 1.5, which is obtained from the literature[30)]. The resultant shape is shown in **Fig. 17**. The RMS errors of zenith angle and height were 10° and 1.1 mm, respectively.

Next, we determined the shape of the bell-shaped object shown in Fig. 7. The object was made of acrylic and its refractive index was 1.5, obtained from the literature[30)]. The diameter (width) of the object was 24 mm and the height was 8 mm. We tilted the object approximately 8 degrees and obtained the data from two views. **Figure 18** shows the rendered image of the estimated shape of the object. **Figure 19** illustrates how the estimated shape fitted the true shape. Dots represent the obtained height and a solid line represents the true value, which was obtained by hand using the edge from the photo of the object observed from the side. The error (mean deviation) in the height was 0.4 mm.

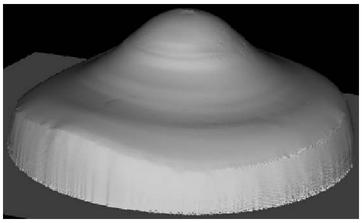

Fig. 18 A rendered image of the obtained shape of the bell-shaped object.

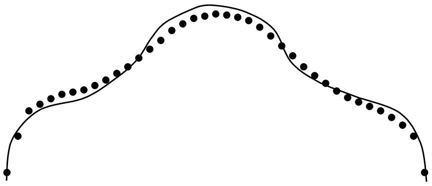

Fig. 19 The result of the real bell-shaped object.

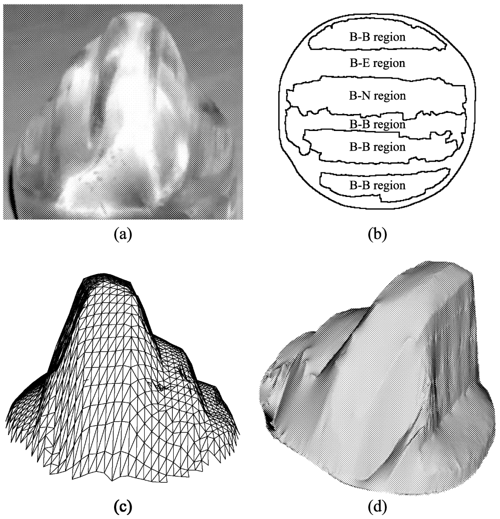

(a) (b)

(c) (d)

Fig. 20 Measurement result of transparent mountain-shaped object: (a) Real image, (b) region segmentation result, and (c) and (d) rendered image.

Another transparent object shown in **Fig. 20** (a) was measured. This mountain-shaped object was made of epoxy and its refractive index was 1.6 [30]. The diameter (width) of the object was 45 mm and the height was 25 mm. Figure 20 (b) shows the result of region segmentation. Here, one B-E region, one B-N region, and four B-B regions are observed. We rotated the object approximately 8 degrees. Figure 20 (c) and Fig. 20 (d) represent the estimated shape of the object.

The software we developed for this second method can be divided into many functions: Computing the DOP from images, segmenting regions, finding corresponding points, computing the zenith angle, computing height from surface normal, and so on. Region segmentation and height computation are performed by the two most complex modules, which take considerable time to compute. Region segmentation took 6.3 [sec] with 85,980 pixels, using a Pentium4 3.4 GHz processor. Here, we employed a simple "region growing" algorithm for implementing the region segmentation. The target object was the mountain-shaped object. We computed height from surface normal by using the alternating-direction implicit method [26] (Section 5.1), and it took 1.6 [sec] with the same number of pixels and the same processor. Since the first method does not need region segmentation, the whole computation speed is faster than the second method.

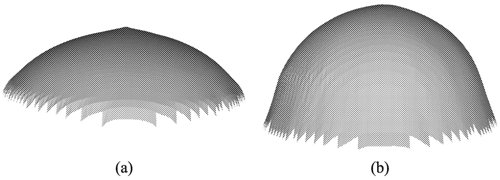

(a) (b)

Fig. 21 3D hemispherical object result: (a) Initial state, (b) Result after 10 loops.

6.5 Experimental Results of the Inverse Polarization Raytracing Method

This section shows the experimental results of the third method, which uses polarization raytracing.

We observed an acrylic transparent hemisphere from the spherical part, whose refractive index was 1.5 and diameter was 30 mm (Fig. 14 (b)). The frontal surface was a hemisphere and the rear surface was a disk. The camera was set orthogonally to the disk. We assumed that the illumination distribution is known.

The estimation result is shown in **Fig. 21**. Figure 21 (a) represents the initial value. We used the result of Saito's method [9], the first method (Section 3), or the second method (Section 4). The shape of these three methods are almost the same because all of them compute the surface normal from the DOP considering only the reflection. The difference between them is only the disambiguation method. If these methods worked perfectly for noiseless data, the results will be exactly the same. Here, we solved the ambiguity problem manually, which is the same approach used with Saito's method. In the following sentences, we

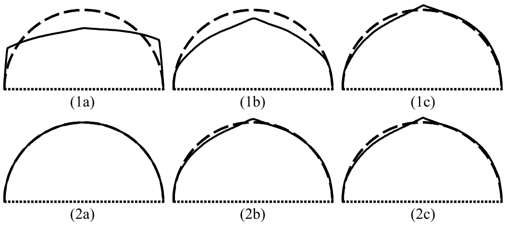

Fig. 22 Estimation result: (1a) Initial state (result of Saito's method), (1b)(1c) Results after 5 and 50 loops, (2a) Initial state (true shape), (2b)(2c) Results after 5 and 50 loops.

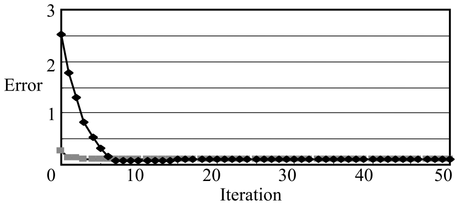

Fig. 23 Error for each loop: (black diamond) Result when initial value is the result of Saito's method, (gray square) result when initial value is the true shape.

use the term "the result of Saito's method" to refer to the result of these three methods. Figure 21 (b) is the result after 10 loops of the method. The computation time was 36 [sec] for 1 loop with 7,854 pixels using a Pentium4 3.4 GHz processor. Here, the maximum number of the light rays traced is 10 reflections or transmissions. However, if the energy of the light ray becomes less than a certain threshold, the tracing of the light ray is stopped.

In order to evaluate the estimation results in more detail, another evaluation was done in the 2D plane. This was a cross-section of the 3D object, which included the center of the base circle and the line perpendicular to that circle. A light ray that was inside this plane did not go out, and a light ray that was outside this plane did not come in. The proposed algorithm estimated the frontal surface shape, a semicircle, by using the polarization data of the 2D plane as input data.

The result of applying the proposed method is given in **Fig. 22** (1c) and Fig. 22 (2c). In Fig. 22, the solid line represents the estimated shape, and the dotted line represents the true shape. For the estimated result shown in Fig. 22 (1c), the result of Saito's method (Fig. 22 (1a)) is used for the initial state of the shape. For the estimated result shown in Fig. 22 (2c), the true shape, hemisphere (Fig. 22 (2a)), is used for the initial state of the shape. Figure 22 (1b)(2b) and Fig. 22 (1c)(2c) are the result after 5 and 50 loops, respectively. The shapes converge to the same shape even if the initial shapes are different.

The value of the cost function (Eq. (28)) per each iteration is plotted in **Fig. 23**. The vertical axis in Fig. 23 represents the value of Eq. (28), while the horizontal axis represents the iteration number. A black diamond mark is the value of the result whose initial state is the result of Saito's method (Fig. 22 (1a)(1b)(1c)). A gray square mark is the value of the result whose initial state is the true shape (Fig. 22 (2a)(2b)(2c)). The leftmost value is the value of the cost function of the initial state. Both the value and the shape did not change after approximately 8 loops.

The computation time was 5.9 [sec] for 1 loop with 320 pixels, using a Pentium4 3.4 GHz processor. Here, the maximum number of the light rays traced is 100 reflections or transmissions. However, if the energy of the light ray becomes less than a certain threshold, the tracing of the light ray is stopped.

The RMS error between the estimated value and the true value is used to compare the accuracy between the proposed method and Saito's method. The RMS error of the zenith angle of the surface normal was 23° for Saito's method, 9.1° for our method when the initial state was the result of Saito's method, and 8.9° for our method when the initial state was the true shape. The RMS error of the height was 2.7 mm for Saito's method, 0.67 mm for our method when the initial state was the result of Saito's method, and 0.55 mm for our method when the initial state was the true shape.

Next, we applied the method to the bell-shaped transparent object shown in Fig. 7. The object was observed from the protruding part of the object. The frontal surface was the curved surface and the rear surface was a disk. The camera was set orthogonally to the disk. We assumed that the illumination distribution was known. We estimated the shape of the cross-section of the object to analyze the precision of the proposed method. **Figure 24** illustrates the estimated shape of the object. The solid curve represents the obtained frontal height, and the dotted line represents the given rear height. The initial value was set to be a semicircle shown in Fig. 24 (a). The estimated shape after 1, 5, and 20 loops is illustrated in

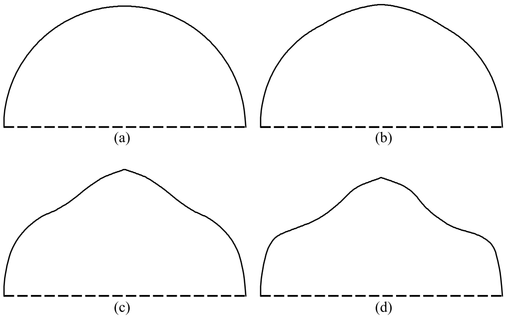

Fig. 24 Estimated shape of bell-shaped acrylic object by using the inverse polarization raytracing method: (a) initial value, (b)(c)(d) estimated after 1, 5, and 20 loops, respectively.

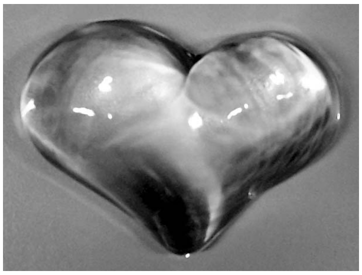

Fig. 25 A photograph of the heart-shaped object.

Fig. 24 (b), (c), and (d), respectively. The true shape is represented as a solid curve in Fig. 19. An error (mean deviation) of the height was 0.24 mm. The computation time was 7.0 [sec] for 1 loop with 320 pixels, using a Pentium4 3.4 GHz processor.

We also applied the method to the heart-shaped transparent object shown in **Fig. 25**. The object was made of glass and its refractive index was 1.5, obtained from the literature[30]. The object was observed from the curved surface of the object. The frontal surface was the curved surface, and the rear surface was a planar surface. The camera was set orthogonally to the rear surface. We assumed that the illumination distribution was known. The estimation result is shown in **Fig. 26**. Figure 26 (a) represents the result of Saito's method and, at the same time, it represents the initial value. Figure 26 (b) is the result after 10 loops of the method. Figure 26 (c) is the rendered example of the raytracing method by using the estimated shape.

7. Discussions

7.1 Discussion of the First Method

Experimental results of the first method proposed in Section 3 are shown in Section 6.3.

The method is applicable to transparent objects that have a complex shape such as shell-like shape.

The resultant shape has some noise at the part whose zenith angle θ is around 0°, points where the surface normal is heading towards the camera. This is caused by the hole on top of the spherical diffuser, a white plastic sphere surrounding the target object. This hole is necessary for the camera to observe the target object. The target object is illuminated by the spherical diffuser except for this hole. Therefore, the surface normal heading towards the camera is noisy because the light is not illuminated at such surface points.

7.2 Discussion of the Second Method

Experimental results of the second method proposed in Section 4 are shown in Section 6.4.

This second method, like the first method, does not consider the influence of internal interreflection, and thus provides an incorrect result.

This second method depends on the robustness of the region segmentation method. Due to the noise caused by internal interreflection, robust region segmentation is difficult. Therefore, this method cannot estimate the shape of a shell-like object, because this object has a complex shape, and region segmentation cannot be achieved so robustly.

The purpose of the first method and the second method is the same; they concentrate on solving the ambiguity problem. These two methods yield a pair of possible surface normals, whose values are the same. But although the resultant surface normals seem to be the same, they are not strictly the same. The first method does not require region segmentation, while the second method does. Therefore, the resultant shapes differ between these methods depending on the result of region segmentation. In most cases, the resultant shape of the first method is more precise than that of the second method due to the difficulty of region segmentation.

7.3 Discussion of the Third Method

Experimental results of the third method proposed in Section 5 are shown in Section 6.5.

This third method requires knowledge of the illumination distribution that surrounds the target object. Correct illumination distributions are needed to recover the error of this surface normal.

The input polarization data is polluted by

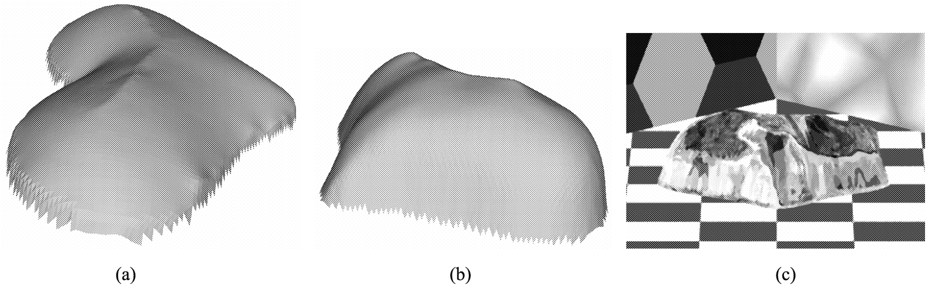
(a) (b) (c)

Fig. 26 Result of heart-shaped object: (a) Initial state, (b) result after 10 loops, (c) raytraced image.

some noise due to the variation of the refractive index inside the object or the opacity of the object. If the variation of the refractive index and the opacity are known, the result will be more precise; however, such information is hard to obtain. In order to reduce such noise, multiple input data are needed, taken under different illumination or taken from different directions.

This third method requires much computation time for iterative computation due to the raytracing method, which takes a great deal of computing time. The region segmentation of the second method takes 6.3 [sec] with 85,980 pixels, while the inverse raytracing of the third method takes 36 [sec] for 1 iteration with 7,854 pixels. Speeding up the computation will be our future work.

If the initial shape is not appropriate, the iteration process will fall to a local minimum. As for the second method, two possible shapes are produced per one B-B region. If these two possible shapes are used as the initial shape, these shapes converge to two different shapes; one is correct and one is incorrect. If the initial shape is similar to the true shape, then it will converge to a correct shape, but if the initial shape is similar to the wrong shape, which is produced by the ambiguity of the degree of the polarization, then it will converge to an incorrect shape. Experimental results shown in Figs. 22 and 23 tell us that the algorithm has a robust convergence if the initial shape is close to the global minimum.

In Section 6.5, the experiment results show that the third method produces a more precise shape than those of the first and second methods. The RMS error of the surface normal for the first and second methods was 23°, while that for the third method was 9.1°, when measuring the transparent hemisphere.

7.4 Discussion of the Result of Hemisphere

We applied the three methods to an acrylic hemispherical object, and calculated the error value for each experiment. Section 6.3 gives the result of the first method, Section 6.4 gives the result of the second method, and Section 6.5 gives the result of the third method. These data are obtained on different dates and under different circumstances; thus, the input data is not the same for each experiment. We cannot compare the effectiveness of each method from these three results. However, Section 6.5 provides a fair comparison between the three methods by analyzing the results produced by the same input data. Section 6.5 indicates that the error for the first and second methods was 23°, and the error for the third method was 9.1°. Therefore, we insist that the third method produces a better shape than the first and second methods.

The error shown in Section 6.3 was 5.9°, the error shown in Section 6.4 was 10°, and the error shown in Section 6.5 was 9.1°. In Section 6.4 and Section 6.5, we used a closed hemisphere, an object whose rear surface is a plane. In Section 6.3, we used an open hemisphere, a thin object whose rear surface is almost the same shape as the frontal surface and is very close to the frontal surface with a width of less than 0.1 mm. This open hemisphere shows less interference from the rear surface, since the surface normal of frontal surface and the rear surface is the same. The DOP is almost the same whether we consider the internal interreflection or not. Therefore, Section 6.3 provides a good result. A closed hemisphere is much more affected by internal interreflection. The internal interreflection causes a large error, like 23° as shown in Section 6.5. In Section 6.4, we increased the DOP value so that the maximum of the observed DOP was equal to 1, since the object always has Brewster points and the maximum DOP should be 1. The error decreased to 10°, as shown in Section 6.4. Section 6.5 considers the internal interreflection by using the polarization raytracing algorithm, and provides a better result. The error was 9.1° as shown in Section 6.5, which is better than 23°. Though the error 10° in Section 6.4 and the error 9.1° in Section 6.5 are only slightly different, the shape obtained by the third method (Fig. 21) looks better than the shape obtained by the second method (Fig. 17).

7.5 Discussion of the Three Methods

Advantages and disadvantages are listed in **Table 1**. The first method analyzes the polarization data in a visible light domain and an infrared light domain; thus, the method uses one visible light camera and one infrared light camera. The second method analyzes the polarization data obtained from two different views; thus, the method uses two visible light cameras, though we actually used one camera by rotating the object. The third method analyzes the polarization data obtained by one visible light camera. The third method provides precise estimation results by considering internal interreflections, while the first and the second methods do not. The third method estimates the object's shape by an iterative computation; thus, it requires an initial value of the object's shape, it takes a great deal of time to compute, and it is not so robust because it falls to a local minimum if the initial value is not good. The first and the second methods do not need an initial value and do not take so much time to compute. The second method is not so robust because it needs region segmentation, which is sensitive to noise, while the first method is robust because it does not need region segmentation or iterative computation. The experimental setup we used cannot measure polarization data in real time; however, some researchers proposed real-time measurement systems[34)~36)]. By using such real-time measurement equipment, the three proposed systems can possibly obtain the polarization data in real time. However, the first method needs to observe the object from one direction with two different cameras; thus, it is difficult using this method to measure the polarization data in real time.

The proposed three methods have both advantages and disadvantages as listed in Table 1.

Table 1 Advantage and disadvantage of three methods.

	Method 1 (infrared)	Method 2 (geometry)	Method 3 (raytracing)
Camera	1 visible 1 infrared	2 visible	1 visible
Accuracy	low	low	high
Robustness	high	low	low
Computation time	quick	quick	long
Possibility of realtime measurement	NG	OK	OK
Initial value	no need	no need	need
Smooth surface (C^2) measurable?	yes	yes	yes
Smooth surface (C^1) measurable?	yes	possibly	yes
Continuous surface (C^0) measurable?	possibly	no	possibly
Discontinuous surface measurable?	no	no	no

Thus, the best way to use these methods depends on the individual circumstances of each case. According to this table, examples of the usage of these methods will be like this:

- If you need a precise shape of a transparent object, then use the third method, which uses the polarization raytracing method (Section 5).
- If you need the shape of a transparent object quickly, then use the second method, with two cameras, which uses the differential geometrical property (Section 4).
- If you are intending to obtain the geometric data of a complex-shaped transparent object, and if the above two methods cannot calculate the complex shape, then use the first method, which uses thermal radiation (Section 3).

However, the third method requires that the rear surface shape is known, and the first method cannot measure an object that deforms with heat.

There is no doubt that we can generate a better method by combining these three methods. Here, we will discuss the characteristics of the combination of the two methods chosen from the three methods.

Method 1 & Method 2 We will have two input data sets taken from two different views. By applying the first method for each data set, we will obtain two shapes. By aligning these two shapes, we will obtain dense correspondences between them. The second method produces better results by using such dense correspondences. The shape will be improved by combining the results from the first method and the second method.

Method 1 & Method 3 Thermal radiation is emitted from the frontal surface, and is subject to less interference by internal interreflection. Analyzing only the thermal radiation provides the true shape of the frontal surface if there is no noise in the input data. If we have a true shape of the frontal surface, the third method can possibly estimate the rear surface, overcoming the problem that the rear surface shape cannot be estimated. However, we have not checked the convergence for this case. If the rear surface shape is given, the third method produces more precise shape by considering the input data from both reflection and thermal radiation.

Method 2 & Method 3 By using two input data sets taken from two different views, the third method can possibly estimate both the frontal surface shape and the rear surface shape. However, we have not checked the convergence for this case. We can use the two shapes produced by the second method as initial values for the third method. The third method improves these two shapes. From the dense correspondences between these two shapes, the second method can check and modify the disambiguation results. We will obtain a precise shape from the third method by combining both shapes.

8. Conclusion

8.1 Summary

In this paper, we have proposed three methods for determining the shape of a transparent object by using a polarization filter. An algorithm that uses only one view in a visible light domain results in ambiguities. The first method solves this ambiguity problem by employing polarization in an infrared light domain, and the second method solves it by employing polarization of a slightly tilted view. These two methods still have a problem in that they do not consider the internal interreflection. The third method solves this internal interreflection problem by employing the polarization raytracing algorithm. The ambiguity problem and the polarization raytracing algorithm are presented in Section 2.

First method 31) Thermal radiation, which also has characteristics of polarization, can be observed as infrared light. This polarization is a one-valued function; measuring the degree of polarization in an infrared domain provides the unique zenith angle. However, the degree of polarization is relatively low, and in some cases it is difficult to determine the degree of polarization precisely. Therefore, we propose to use polarization in both visible and infrared light. This method is presented in Section 3.

Second method 32) By rotating the object, the ambiguity problem can be also solved. Two sets of data are obtained: one is from the object not tilted, and the other is from the object tilted at a small angle. These data are segmented into regions with regard to the Brewster angle. Then, the method calculates the difference of the degree of polarization between these two sets of data at the corresponding point — the point where surface normal lies along the rotation direction and where the degree of polarization is minimum in the B-B region. From that difference, the correct surface normal is determined. This method is presented in Section 4.

Third method 33) Solving the inverse problem of the polarization raytracing method, the shape of transparent objects can be estimated more precisely. The polarization raytracing method considers internal interreflection. To obtain the shape of a transparent object, the method minimizes the difference between the input polarization data taken by observing the transparent object and the computed polarization data rendered by the polarization raytracing method. This method is presented in Section 5.

We have implemented these proposed methods, and demonstrated their abilities to determine the shape of transparent objects. Experiments are presented in Section 6.

8.2 Future Work

Our future work is to obtain the shapes of transparent objects more accurately. We also intend to develop a method that can measure the refractive index at the same time as well as the surface shape of transparent object. We have developed a polarization camera 37), which measures the polarization state of the light, and we are now trying to improve it so that it can measure at a faster speed than the existing real-time polarization camera 34)~36). Another future work is to develop a commercial product for measuring the shape of transparent objects by collaborating with a camera manufacturer. We are also planning to collaborate with physicists to make our methods more robust by using their specialized knowledge.

There are many beautiful glass objects of art in all over the world. The proposed method will be useful for modeling such glass objects of art. Other application fields that can benefit from the modeling of transparent objects might include computer-aided manufacturing, classifying garbage/rubbish for recycling glass and plastic bottles, and creating 3D catalogs for online shopping. As the first step for such a wide area of applications, we proposed a basic technique for modeling the surface shape of transparent objects.

Acknowledgments This research was supported in part by the Japan Science and Technology Agency under the Ikeuchi CREST project and in part by the Ministry of Education, Culture, Sports, Science and Technology under the Leading Project, "Development of High Fidelity Digitization Software for Large-Scale and Intangible Cultural Assets." Daisuke Miyazaki was supported in part by the Japan Society for the Promotion of Science. This research was performed in part in collaboration with Megumi Saito, Masataka Kagesawa, and Yoichi Sato. The authors thank Joan Knapp for proofreading and editing this manuscript.

References

1) Koshikawa, K. and Shirai, Y.: A model-based recognition of glossy objects using their polarimetrical properties, *Advanced Robotics*, Vol.2, No.2, pp.137–147 (1987).

2) Wolff, L.B. and Boult, T.E.: Constraining object features using a polarization reflectance model, *IEEE Trans. Pattern Analysis and Machine Intelligence*, Vol.13, No.7, pp.635–657 (1991).

3) Rahmann, S.: Inferring 3D Scene Structure from a Single Polarization Image, *SPIE Proc. Conf. Polarization and Color Techniques in Industrial Inspection*, Vol.3826, pp.22–33 (1999).

4) Rahmann, S.: Polarization images: a geometric interpretation of shape analysis, *Proc. Int'l Conf. Pattern Recognition*, pp.542–546 (2000).

5) Rahmann, S. and Canterakis, N.: Reconstruction of specular surfaces using polarization imaging, *Proc. Int'l Conf. Computer Vision and Pattern Recognition*, pp.149–155 (2001).

6) Rahmann, S.: Reconstruction of quadrics from two polarization views, *Proc. Iberian Conf. Pattern Recognition and Image Analysis*, pp.810–820 (2003).

7) Drbohlav, O. and Šára, R.: Unambiguous determination of shape from photometric stereo with unknown light sources, *Proc. IEEE Int'l Conf. Computer Vision*, pp.I:581–586 (2001).

8) Miyazaki, D., Tan, R.T., Hara, K. and Ikeuchi, K.: Polarization-based inverse rendering from a single view, *Proc. IEEE Int'l Conf. Computer Vision*, pp.982–987 (2003).

9) Saito, M., Sato, Y., Ikeuchi, K. and Kashiwagi, H.: Measurement of surface orientations of transparent objects by use of polarization in highlight, *J. Optical Society of America, A*, Vol.16, No.9, pp.2286–2293 (1999).

10) Murase, H.: Surface shape reconstruction of a nonrigid transparent object using refraction and motion, *IEEE Trans. Pattern Analysis and Machine Intelligence*, Vol.14, No.10, pp.1045–1052 (1992).

11) Hata, S., Saitoh, Y., Kumamura, S. and Kaida, K.: Shape extraction of transparent object using genetic algorithm, *Proc. Int'l Conf. Pattern Recognition*, pp.684–688 (1996).

12) Ohara, K., Mizukawa, M., Ohba, K. and Taki, K.: 3D modeling of micro transparent object with integrated vision, *Proc. IEEE Conf. Multisensor Fusion and Integration for Intelligent Systems*, pp.107–112 (2003).

13) Ben-Ezra, M. and Nayar, S.K.: What does motion reveal about transparency?, *Proc. IEEE Int'l Conf. Computer Vision*, pp.1025–1032 (2003).

14) Kutulakos, K.N. and Steger, E.: A theory of refractive and specular 3D shape by light-path triangulation, *Proc. IEEE Int'l Conf. Computer Vision*, pp.1448–1455 (2005).

15) Morris, N. and Kutulakos, K.N.: Dynamic refraction stereo, *Proc. IEEE Int'l Conf. Computer Vision*, pp.1573–1580 (2005).

16) Born, M. and Wolf, E.: *Principles of optics*, p.803, Pergamon Press (1959).

17) Shurcliff, W.A.: *Polarized light: production and use*, p.207, Harvard University Press (1962).

18) Sandus, O.: A review of emission polarization, *Applied Optics*, Vol.4, No.12, pp.1634–1642 (1965).

19) Nicodemus, F.E.: Directional reflectance and emissivity of an opaque surface, *Applied Optics*, Vol.4, pp.767–773 (1965).

20) Nicodemus, F.E.: Reflectance nomenclature and directional reflectance and emissivity, *Applied Optics*, Vol.9, pp.1474–1475 (1970).

21) Jordan, D.L. and Lewis, G.D.: Measurements of the effect of surface roughness on the polarization state of thermally emitted radiation, *Optical Letters*, Vol.19, pp.692–694 (1994).

22) Jordan, D.L., Lewis, G.D. and Jakeman, E.: Emission polarization of roughened glass and aluminum surfaces, *Applied Optics*, Vol.35, pp.3583–3590 (1996).

23) Wolff, L.B., Lundberg, A. and Tang, R.: Image

understanding from thermal emission polarization, *Proc. IEEE Conf. Computer Vision and Pattern Recognition*, pp.625–631 (1998).
24) do Carmo, M.P.: *Differential geometry of curves and surfaces*, p.503, Prentice-Hall (1976).
25) Horn, B.K.P.: *Robot vision*, p.509, MIT Press (1986).
26) Press, W.H., Teukolsky, S.A., Vetterling, W.T. and Flannery, B.P.: *Numerical recipes in C: the art of scientific computing*, p.994, Cambridge University Press (1992).
27) Courant, R. and Hilbert, D.: *Methods of mathematical physics*, p.575, Wiley-Interscience (1989).
28) Ikeuchi, K.: Reconstructing a depth map from intensity maps, *Proc. Int'l Conf. Pattern Recognition*, pp.736–738 (1984).
29) Horn, B.K.P.: Height and Gradient from Shading, *Int'l J. Computer Vision*, Vol.5, No.1, pp.37–75 (1990).
30) Shackelford, J.F., Alexander, W. and Park, J.S.: *CRC Materials Science and Engineering Handbook*, p.883, CRC Press (1994).
31) Miyazaki, D., Saito, M., Sato, Y. and Ikeuchi, K.: Determining surface orientations of transparent objects based on polarization degrees in visible and infrared wavelengths, *J. Optical Society of America, A*, Vol.19, No.4, pp.687–694 (2002).
32) Miyazaki, D., Kagesawa, M. and Ikeuchi, K.: Transparent surface modeling from a pair of polarization images, *IEEE Trans. Pattern Analysis and Machine Intelligence*, Vol.26, No.1, pp.73–82 (2004).
33) Miyazaki, D. and Ikeuchi, K.: Inverse Polarization Ray-tracing: Estimating Surface Shape of Transparent Objects, *Proc. Int'l Conf. Computer Vision and Pattern Recognition*, pp.II:910–917 (2005).
34) Wolff, L.B., Mancini, T.A., Pouliquen, P. and Andreou, A.G.: Liquid Crystal Polarization Camera, *IEEE Trans. Robotics and Automations*, Vol.13, No.2, pp.195–203 (1997).
35) Fujikake, H., Takizawa, K., Aida, T., Kikuchi, H., Fujii, T. and Kawakita, M.: Electrically-Controllable Liquid Crystal Polarizing Filter for Eliminating Reflected Light, *Optical Review*, Vol.5, No.2, pp.93–98 (1998).
36) Harnett, C.K. and Craighead, H.G.: Liquid-crystal micropolarizer array for polarization-difference imaging, *Applied Optics*, Vol.41, No.7, pp.1291–1296 (2002).
37) Miyazaki, D., Takashima, N., Yoshida, A., Harashima, E., Ikeuchi, K.: Polarization-based Shape Estimation of Transparent Objects by Using Raytracing and PLZT Camera, *Proc. SPIE*, pp.1–14 (2005).

(Received September 1, 2005)
(Accepted March 17, 2006)

(Editor in Charge: *Yasunari Kameda*)

Daisuke Miyazaki received a B.S. degree in science from the University of Tokyo in 2000, an M.S. degree in information science and technology from the University of Tokyo in 2002, and a Ph.D. degree in information science and technology from the University of Tokyo in 2005. He is a post-doctoral researcher at the University of Tokyo, Japan. He received the Best Overall Paper Award from VSMM in 2000. His research interests include physics-based vision and image-based modeling. He is a member of the IEEE.

Katsushi Ikeuchi received a B. Eng. degree in mechanical engineering from Kyoto University, Kyoto, Japan, in 1973, and a Ph.D. degree in information engineering from the University of Tokyo, Tokyo, Japan, in 1978. He is a professor at the Interfaculty Initiative in Information Studies, the University of Tokyo, Tokyo, Japan. After working at the AI Laboratory at the Massachusetts Institute of Technology for three years, the Electrotechnical Laboratory for five years, and the School of Computer Science at Carnegie Mellon University for 10 years, he joined the University of Tokyo in 1996. He was selected as a Distinguished Lecturer of the IEEE Signal Processing Society for the period of 2000–2001, and a Distinguished Lecturer of the IEEE Computer Society for the period of 2004–2006. He has received several awards, including the David Marr Prize in ICCV 1990, IEEE R&A K-S Fu Memorial Best Transaction Paper Award in 1998, and best paper awards in CVPR 1991, VSMM 2000, and VSMM 2004. In addition, in 1992, his paper, "Numerical Shape from Shading and Occluding Boundaries," was selected as one of the most influential papers to have appeared in the Artificial Intelligence Journal within the past 10 years. He is a fellow of the IEEE.